

Enhanced peak growth of global vegetation and its key mechanisms

Kun Huang^{1,2}, Jianyang Xia^{1,2*}, Yingping Wang^{3,4}, Anders Ahlström^{5,6}, Jiquan Chen⁷, Robert B. Cook⁸, Erqian Cui¹, Yuanyuan Fang⁹, Joshua B. Fisher¹⁰, Deborah Nicole Huntzinger¹¹, Zhao Li¹, Anna M. Michalak⁹, Yang Qiao¹, Kevin Schaefer¹², Christopher Schwalm¹³, Jing Wang¹, Yaxing Wei⁸, Xiaoni Xu¹, Liming Yan^{1,14}, Chenyu Bian¹ and Yiqi Luo¹⁵

The annual peak growth of vegetation is critical in characterizing the capacity of terrestrial ecosystem productivity and shaping the seasonality of atmospheric CO₂ concentrations. The recent greening of global lands suggests an increasing trend of terrestrial vegetation growth, but whether or not the peak growth has been globally enhanced still remains unclear. Here, we use two global datasets of gross primary productivity (GPP) and a satellite-derived Normalized Difference Vegetation Index (NDVI) to characterize recent changes in annual peak vegetation growth (that is, GPP_{max} and NDVI_{max}). We demonstrate that the peak in the growth of global vegetation has been linearly increasing during the past three decades. About 65% of the NDVI_{max} variation is evenly explained by expanding croplands (21%), rising CO₂ (22%) and intensifying nitrogen deposition (22%). The contribution of expanding croplands to the peak growth trend is substantiated by measurements from eddy-flux towers, sun-induced chlorophyll fluorescence and a global database of plant traits, all of which demonstrate that croplands have a higher photosynthetic capacity than other vegetation types. The large contribution of CO₂ is also supported by a meta-analysis of 466 manipulative experiments and 15 terrestrial biosphere models. Furthermore, we show that the contribution of GPP_{max} to the change in annual GPP is less in the tropics than in other regions. These multiple lines of evidence reveal an increasing trend in the peak growth of global vegetation. The findings highlight the important roles of agricultural intensification and atmospheric changes in reshaping the seasonality of global vegetation growth.

The temporal dynamics of atmospheric CO₂ concentrations ([CO₂]) are inversely correlated with that of terrestrial CO₂ uptake^{1,2} and vegetation growth^{3–7}. Atmospheric monitoring has revealed an increase of 30–60% in the seasonal amplitude of CO₂ concentrations over the Northern Hemisphere since the 1960s^{8,9}. The enhanced seasonal CO₂ amplitude is largely driven by the increasing drawdown of the trough of the CO₂ seasonal cycle in the Northern Hemisphere during summer, when CO₂ uptake resulting from vegetation growth also peaks. There is also recent evidence that the interannual variation of terrestrial net carbon uptake correlates more strongly with the peak gross primary productivity (GPP) than any climatic factors^{10–12}. In addition, global lands have been greening since the 1980s^{13,14}. All of these lines of evidence imply an increasing peak growth of vegetation, but whether such a trend exists globally or mainly in some specific regions remains unknown. A continuing increase of peak vegetation growth is ecologically possible, because measurements of modern-plant traits have found large variations in leaf photosynthetic capacity among and within plant functional types¹⁵, and palaeoecological studies

have revealed high variability in the maximum individual size of vascular plants under different climatic regimes¹⁶. Thus, to better predict the temporal trends of land-sink capacity and atmospheric [CO₂] dynamics, we need to examine whether the peak growth of global vegetation has been enhanced in past years, and understand the global distributions of the change in peak vegetation growth and their driving factors.

Here, we examine the trends of peak vegetation growth using two proxies—the maximum monthly GPP (GPP_{max}) and maximum monthly Normalized Difference Vegetation Index (NDVI_{max})—and identify their key driving factors. The global-scale GPP dataset was derived by a machine-learning technique known as the model tree ensemble (MTE) using FLUXNET measurements¹⁷. The NDVI data were obtained from Global Inventory Modeling and Mapping Studies (GIMMS) corrected for satellite sensor drift¹⁸. We investigated the difference in photosynthetic capacity among plant functional types using measurements of sun-induced chlorophyll fluorescence (SIF) from Global Ozone Monitoring Experiment 2 (GOME-2)¹⁹, flux-tower measurements from FLUXNET¹⁰ and plant

¹Tiantong National Station of Forest Ecosystem Research, Center for Global Change and Ecological Forecasting, School of Ecological and Environmental Sciences, East China Normal University, Shanghai, China. ²Institute of Eco-Chongming, Shanghai, China. ³CSIRO Oceans and Atmosphere, Melbourne, Victoria, Australia. ⁴Terrestrial Biogeochemistry Group, South China Botanic Garden, Chinese Academy of Sciences, Guangzhou, China. ⁵Department of Physical Geography and Ecosystem Science, Lund University, Lund, Sweden. ⁶Department of Earth System Science, School of Earth, Energy and Environmental Sciences, Stanford University, Stanford, CA, USA. ⁷Center for Global Change and Earth Observations and Department of Geography, Environment, and Spatial Sciences, Michigan State University, East Lansing, MI, USA. ⁸Environmental Sciences Division, Oak Ridge National Laboratory, Oak Ridge, TN, USA. ⁹Department of Global Ecology, Carnegie Institution for Science, Stanford, CA, USA. ¹⁰Jet Propulsion Laboratory, California Institute of Technology, Pasadena, CA, USA. ¹¹School of Earth and Sustainability, Northern Arizona University, Flagstaff, AZ, USA. ¹²National Snow and Ice Data Center, Cooperative Institute for Research in Environmental Sciences, University of Colorado, Boulder, CO, USA. ¹³Woods Hole Research Center, Falmouth, MA, USA. ¹⁴Forest Ecosystem Research and Observation Station in Putuo Island, School of Ecological and Environmental Sciences, East China Normal University, Shanghai, China. ¹⁵Center for Ecosystem Science and Society and Department of Biological Sciences, Northern Arizona University, Flagstaff, AZ, USA. *e-mail: jyxia@des.ecnu.edu.cn

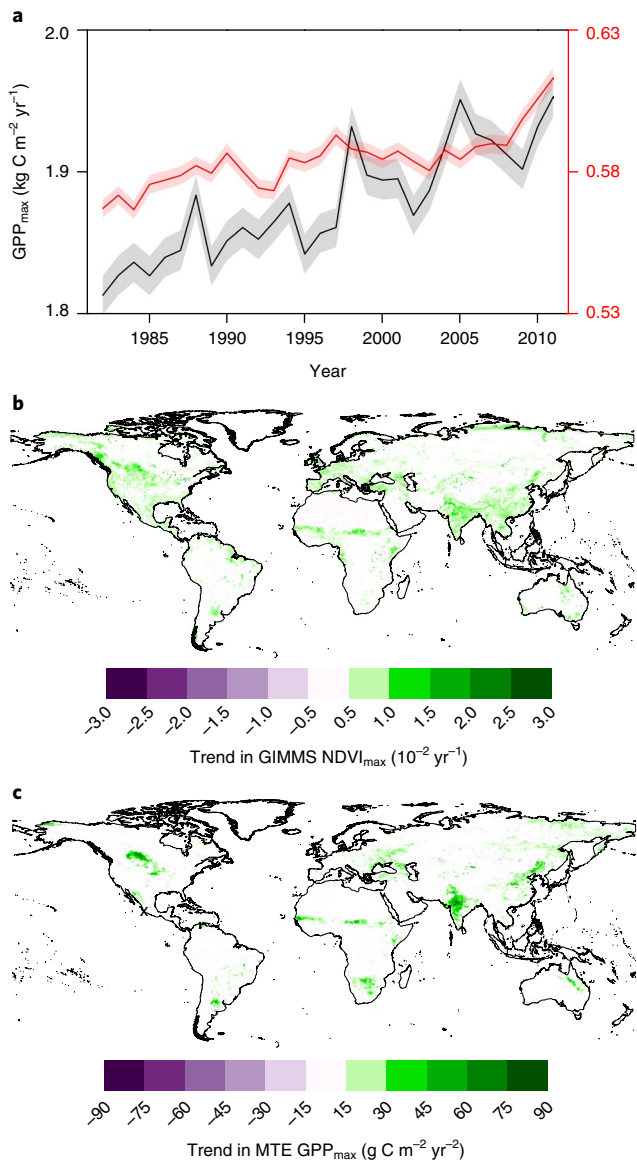


Fig. 1 | Enhanced monthly vegetation growth peak. **a**, Annual time series of MTE GPP_{max} (black line) and GIMMS $NDVI_{max}$ (red line) over 1982–2011. The shaded areas represent one s.e.m. **b, c**, Spatial patterns of the temporal trend in GIMMS $NDVI_{max}$ (**b**) and MTE GPP_{max} (**c**), with white indicating those areas with no significant changes ($P > 0.05$).

functional traits from the TRY database¹⁵ (see Methods). A meta-analysis of 466 experiments was further conducted to compare the contributions of elevated CO_2 , climate warming and nitrogen addition to peak accumulation of plant biomass (see Methods). Finally, using the results of different model scenarios (Supplementary Table 1) from the Multi-scale Synthesis and Terrestrial Model Intercomparison Project (MsTMIP)²⁰, we quantified the contributions of changes in land cover, climate and atmosphere to the simulated trends of global peak GPP.

The two indices of peak vegetation growth across the globe (MTE GPP and NDVI) consistently showed linearly increasing trends during the past three decades (1982–2011), with global trends of MTE GPP_{max} and $NDVI_{max}$ of $3.931 \text{ g C m}^{-2} \text{ yr}^{-2}$ ($P < 0.05$) and 0.0013 yr^{-1} ($P < 0.05$), respectively (Fig. 1a). The observed increase in global averaged MTE GPP_{max} was consistent with the observed growth in atmospheric CO_2 amplitude at Point Barrow (71.3°N , 156.6°W ; $r^2 = 0.32$, $P < 0.01$) (Supplementary Fig. 1). Globally, the

fastest increase in peak vegetation growth occurred in areas of intense agricultural activities, such as northern China, India and North America (Fig. 1b,c and Supplementary Fig. 2). Additionally, the maximum monthly enhanced vegetation index (EVI_{max}) also illustrated increasing trends in these agricultural regions over 2000–2011 (Supplementary Fig. 3).

We then applied a relative importance algorithm (see Methods) to attribute the annual change in $NDVI_{max}$ during 1982–2010 to its drivers (note that we did not attribute MTE GPP_{max} , because climate and land-use data were used as explanatory variables to train MTE GPP). The driving factors included incoming solar radiation, air temperature, annual precipitation, agricultural activities (for example, fractional change of cropland), rising CO_2 and nitrogen deposition. The contribution of each factor was calculated for each grid cell (Supplementary Fig. 4), and the factor that made the greatest contribution to the $NDVI_{max}$ variation was identified as the dominant driver (Fig. 2a). At the global scale, around 65% of $NDVI_{max}$ variation could be explained by the combination of changes in atmospheric $[CO_2]$ (22%), the rate of nitrogen deposition (22%) and cropland fraction (21%) (Fig. 2a). These factors were also the primary explanatory factors along the global latitudinal gradient (Fig. 2b). Although croplands only accounted for around 13.8% of the land area globally (Supplementary Fig. 5a), they contributed to 31.8% of the global increasing GPP_{max} trends (Supplementary Fig. 5b). Also, higher intra-biome fractions of significant GPP_{max} trends were found in croplands compared with other biomes (Supplementary Fig. 5c).

The large contribution of agricultural activities may be related to the higher photosynthetic capacity that crops have over non-crops. Here, we analysed observed multi-level photosynthetic capacity data in three biome groups: cropland, forest and grassland. From 612 observations^{21–23} across 81 species, we found that crops had a higher leaf-level maximum carboxylation rate (V_{cmax}) ($85.2 \pm 31.0 \mu\text{mol m}^{-2} \text{ s}^{-1}$) compared with trees ($56.4 \pm 26.7 \mu\text{mol m}^{-2} \text{ s}^{-1}$) and grasses ($36.9 \pm 27.9 \mu\text{mol m}^{-2} \text{ s}^{-1}$) (Fig. 3a). Ecosystem-level measurements of daily GPP across 125 eddy-flux sites also demonstrated the higher GPP_{max} in cropland ($15.9 \pm 5.6 \text{ g C m}^{-2} \text{ d}^{-1}$) compared with forest ($10.8 \pm 3.6 \text{ g C m}^{-2} \text{ d}^{-1}$) and grassland ($9.0 \pm 4.8 \text{ g C m}^{-2} \text{ d}^{-1}$) (Fig. 3b). At the biome level, the maximum monthly SIF (SIF_{max}), retrieved from the GOME-2 spectral instrument (Fig. 3c), showed that croplands had a higher maximum photosynthetic capacity ($1.6 \pm 0.4 \text{ mW m}^{-2} \text{ sr}^{-1} \text{ nm}^{-1}$) than areas of forest ($1.3 \pm 0.5 \text{ mW m}^{-2} \text{ sr}^{-1} \text{ nm}^{-1}$) and grassland ($1.2 \pm 0.5 \text{ mW m}^{-2} \text{ sr}^{-1} \text{ nm}^{-1}$). These findings were consistent with previous studies that detected a higher maximum photosynthetic capacity in croplands than surrounding dense forests under similar climate conditions^{19,24}.

As shown by the meta-analysis of 466 experiments across 719 plant species (Supplementary Fig. 6), peak accumulation of leaf biomass was significantly enhanced by elevated CO_2 (95% confidence interval (CI): 16.7–24.1%) and nitrogen addition (12.4–18.5%), but to a lesser extent by climate warming (2.3–13.6%) (Fig. 3d). There could be multiple reasons for this. First, the results are consistent with the reported strong, worldwide CO_2 fertilization effect^{25–27} and nitrogen limitation^{28,29} on plant photosynthesis. Second, climate warming benefited plant growth primarily through advancing spring leaf onset³⁰, but could suppress plant peak growth by triggering summer water deficiency in dry years or regions^{31,32}. Warming could also affect plant growth by increasing soil nitrogen mineralization and availability³³. In addition, the effects of elevated CO_2 and nitrogen addition on plant biomass were significant in almost all plant functional types, whereas the warming effect was insignificant for herbs (Supplementary Fig. 7). However, it should be noted that croplands are highly managed by humans, so the difference in environmental contributions in cropland regions is uncertain.

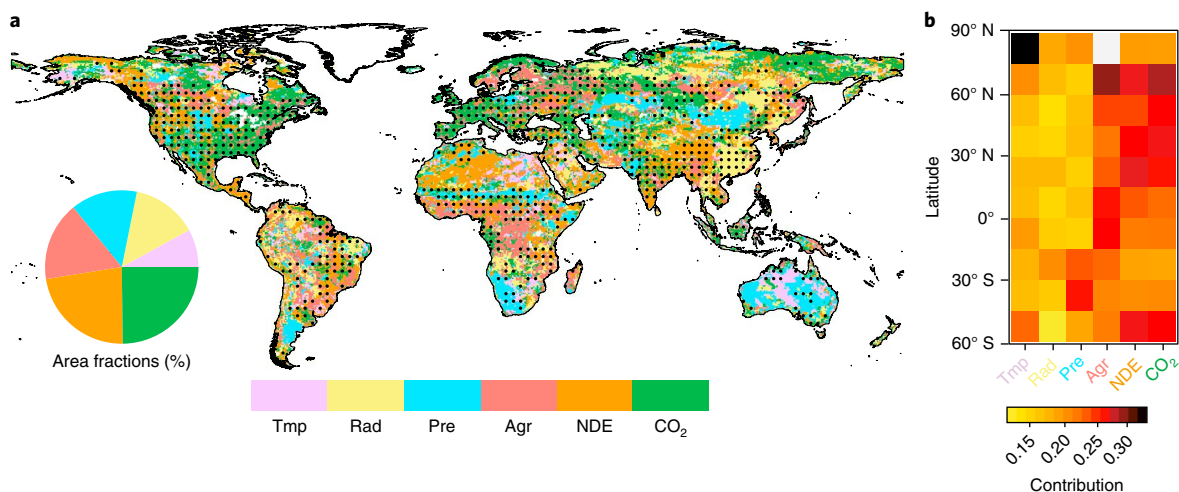


Fig. 2 | Attribution of peak monthly vegetation growth (NDVI_{max}). **a**, The dominant factor influencing variations in NDVI_{max}, defined as the driving factor that contributes the most to the increase (or decrease) in NDVI_{max}, is indicated in each grid cell. The statistically significant regions ($P < 0.05$) are labelled with black dots. The six driving factors include incoming shortwave radiation (Rad), annual average air temperature (Tmp), annual precipitation (Pre), annual agriculture cropland fractional changes (Agr), nitrogen deposition (NDE) and rising CO₂ (CO₂). Inset, pie chart showing the area fractions of lands dominated by each factor. **b**, Contributions of the six driving factors in 15° latitude bands (90°N–60°S).

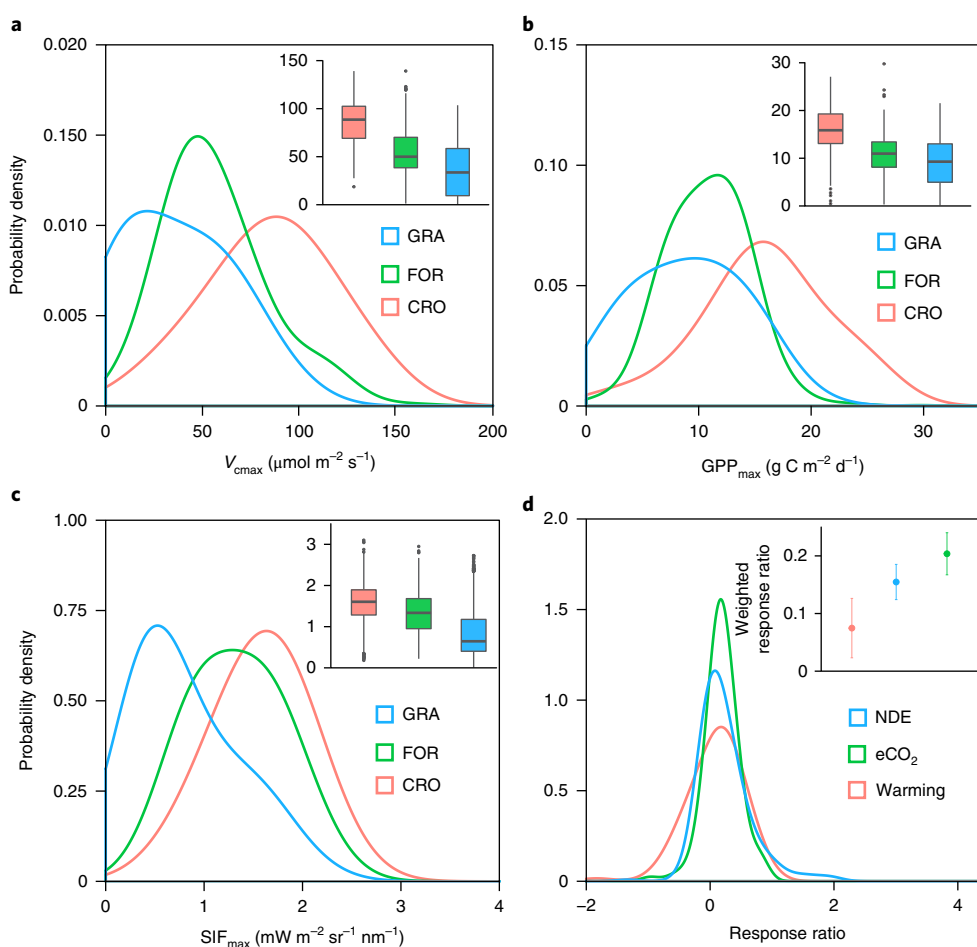


Fig. 3 | Higher photosynthetic capacity of croplands. The probability density functions of three datasets were calculated for cropland (CRO), forest (FOR) and grassland (GRA) ecosystems. **a**, Probability density distributions of photosynthesis capacity by leaf-level V_{cmax} (from the TRY database) for each biome type. **b**, Ecosystem-level flux-tower-based GPP_{max} across the FLUXNET2015 sites. **c**, Biome-level SIF_{max} over 2007–2015 (derived from GOME-2). The inset boxplots in **a–c** show the 25th and 75th percentiles (box edges). Median values are shown by black horizontal bars in each box and the whiskers correspond to 1.5x inter-quartile range. **d**, Probability density functions of natural log-transformed leaf biomass response ratios to nitrogen deposition, elevated CO₂ (eCO₂) and warming treatments. Inset, weighted response ratios \pm 95% CIs of leaf biomass response ratios to the treatments using meta-analysis.

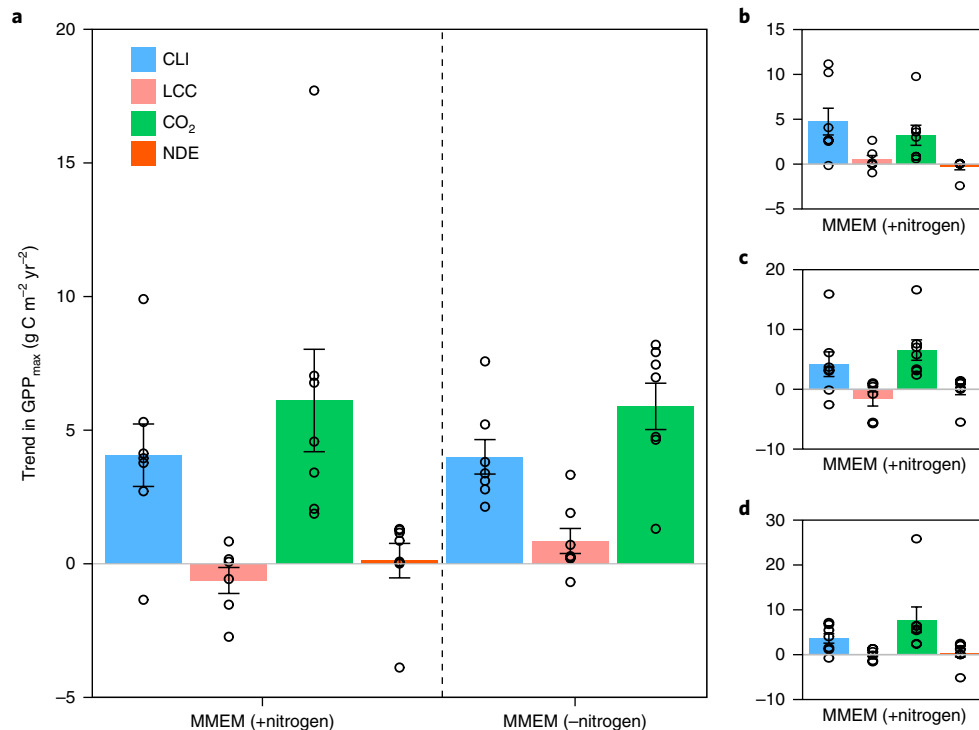


Fig. 4 | Attribution of peak GPP trends (GPP_{max}) using factorial simulations of the ensemble mean of models with (+nitrogen) and without (–nitrogen) a coupled carbon–nitrogen cycle. a–d, Attributions of modelled GPP_{max} trends (g C m⁻² yr⁻²) over the globe (a), northern high latitudes (-60–90° N; b), northern mid-latitudes (-30–60° N; c) and tropics (-0–30° N; d). Modelled trends in GPP_{max} were estimated using the multi-model ensemble mean (MMEM) from the MsTMIP by LCC, nitrogen deposition (NDE), climate change (CLI) and rising CO₂ (CO₂), using a least squares linear regression ($P < 0.05$). The MMEM was calculated in two sub-ensembles: models with nitrogen limitations (+nitrogen) and models without nitrogen limitations (–nitrogen). Error bars show the s.e.m. of GPP_{max} trends derived from the model simulations.

We further examined the temporal trend of GPP_{max} over 1982–2010 using 15 terrestrial biosphere models from the MsTMIP³⁴, and evaluated the ability of these models to project a response of GPP_{max} to climate change (varying temperature, precipitation and radiation), land cover change (LCC), rising CO₂ and nitrogen deposition (Supplementary Figs. 8–11). Globally, CO₂ fertilization and climate change were attributed as primary drivers of the modelled GPP_{max} trend (Fig. 4), although models disagreed on the relative importance of those two drivers (Supplementary Table 2). We note that the influences of nitrogen deposition might be uncertain because only a few models (8 out of 15) in the ensemble incorporated nitrogen limitation. Here, when using the models to perform factorial simulations that include nitrogen deposition, rising CO₂ accounted for $63 \pm 20\%$ (6.2 ± 1.91 g C m⁻² yr⁻²) of the modelled GPP_{max} trend globally, followed by climate change ($42 \pm 12\%$, 4.06 ± 1.17 g C m⁻² yr⁻²), nitrogen deposition ($1 \pm 7\%$, 0.11 ± 0.64 g C m⁻² yr⁻²) and LCC ($-6 \pm 5\%$, -0.63 ± 0.49 g C m⁻² yr⁻²) (Fig. 4a, +nitrogen). Models without carbon–nitrogen couplings demonstrated similar contributions of rising CO₂ and climate change, but positive contributions of LCC to the modelled GPP_{max} trend (rising CO₂: $55 \pm 8\%$, 5.89 ± 0.87 g C m⁻² yr⁻²; climate change: $37 \pm 6\%$, 4 ± 0.64 g C m⁻² yr⁻²; LCC: $8 \pm 4\%$, 0.85 ± 0.47 g C m⁻² yr⁻²). The LCC effect might not be adequately captured by the MsTMIP models since most models do not explicitly represent crops or agricultural management³⁵. Similarly, CO₂ fertilization and climate change effects were the main drivers of the modelled GPP_{max} trend in the three latitude zones (northern high latitudes, mid-latitudes and tropics), with CO₂ fertilization showing the largest contribution ($66 \pm 24\%$) to the tropical GPP_{max} trend (Fig. 4b–d). Examining the correlations of MTE GPP_{max} with cropland fractional changes (Supplementary Fig. 12), modelled LCC effects were consistently underestimated in all of the latitude zones

(Fig. 4b–d). The LCC schemes of the models participating in the MsTMIP varied greatly³⁵, and differences remained in the model processes relating to the LCCs, including cropland conversion. The underestimated LCC effect could also be due to the fact that agricultural management represented by these models differed significantly by the algorithms specified for the major crop types, such as fertilizer applications, irrigation and tillage practices³⁶.

Our study confirms the long-term increase in global vegetation's peak growth during the past three decades. While there is no single driver for the increase in peak vegetation growth, the intensification of agriculture^{24,37} and rapid increases in atmospheric [CO₂]^{13,38} and nitrogen deposition^{29,39} have served as the most important forcing factors. The expansion of cropland is an important driver, because the enhanced GPP_{max} and NDVI_{max} (Fig. 1b,c) are largely located in the regions with increasing cropland fractions (Supplementary Fig. 12). In regions with decreasing cropland fractions; for example, the eastern United States and western Europe (Supplementary Fig. 13), no significantly increasing trends in GPP_{max} and NDVI_{max} were detected (Fig. 1b,c). The cropland expansion also drives the enhanced NDVI_{max} in many tropical regions, partially because their peak vegetation growth is not sensitive to the changes in other factors. For example, the peak growth occurs in dry seasons in many tropical forests with high annual precipitation⁴⁰. The higher peak growth of crops compared with non-crop plants results from not only their larger photosynthetic capacity from leaf to community levels (Fig. 3a–c), but also the intense management (irrigation and fertilization)^{41,42} in croplands during the growing season⁴³, which creates nearly ideal growing conditions that are rare in unmanaged ecosystems. Rising CO₂ largely controls the trends of peak vegetation growth in both satellite-based and modelling analyses.

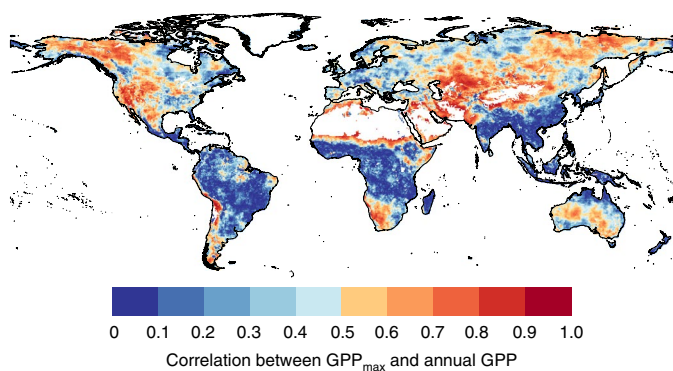


Fig. 5 | Correlation of MTE GPP_{max} with annual GPP. Global distribution of r^2 values between MTE GPP_{max} and annual GPP over 1982–2011.

It supports the recent finding of a linear relationship between GPP responses and seasonal atmospheric CO_2 amplitude in reaction to rising CO_2 ³⁸. The dominant role of rising CO_2 rather than other factors in the eastern United States and western Europe has also been reported as part of the analysis of long-term eddy-flux observations⁴⁴. Because nitrogen is a key factor determining plant photosynthetic capacity^{28,29}, the large contribution of nitrogen deposition to the enhanced peak growth of vegetation is probably related to plant photosynthetic capacity stimulated by leaf nitrogen concentrations⁴⁵.

Large uncertainty in terrestrial productivity simulated by terrestrial biosphere models has been repeatedly documented over the past few decades^{1,46}. This study proposes feasible improvements to ecosystem productivity simulations by emphasizing peak vegetation growth. First, models differ in the design of crop types and the ways in which they deal with crop and agricultural management. MsTMIP models might underestimate the contribution of agricultural activities to the global increase in peak vegetation growth, because most models do not explicitly represent crops and agricultural management³⁵. The findings presented here call for an explicit incorporation of agricultural management—such as planting dates and harvesting strategies, cultivar choices, and fertilizer application and irrigation/tillage practices—in global carbon-cycle models^{47–50}. Second, further model evaluations and improvements in the control of leaf nitrogen concentrations and environmental variables (for example, temperature, radiation, day length and humidity), when modelling plant photosynthetic capacity (for example, V_{cmax}) are needed, as they are conventionally assumed to be constant for each plant functional type or to vary linearly with leaf nitrogen concentrations in current terrestrial biosphere models⁴⁵.

It should be noted that GPP_{max} contributed less to the temporal changes in annual GPP in the tropics than other regions (Fig. 5). However, whether the enhanced peak growth is associated with an increase of global annual GPP remains uncertain. For example, some recent analyses have shown a minor increasing trend of global annual GPP during the past three decades^{14,51}. Also, the efficiency of productivity (for example, the net primary productivity (NPP)-to-GPP ratio) increases with cropland expansion, rising atmospheric $[CO_2]$ and enhanced nitrogen deposition (Fig. 6). Thus, more research efforts are still needed to explore the long-term trend of global NPP, which has been recognized as a measurable planetary boundary for the biosphere⁵².

The global datasets and attribution methods used here have their own uncertainties. Previous studies have revealed that MTE GPP products depend partly on climate and partly on other parameters (for example, the fraction of absorbed photosynthetically active radiation and light-use efficiency). Thus, the study of

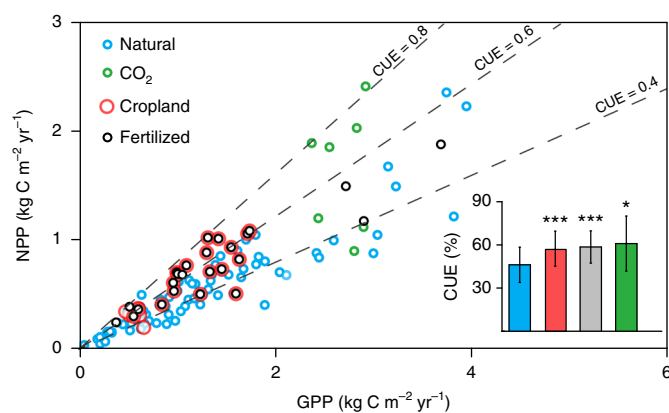


Fig. 6 | Relationship between measured NPP and GPP. Points show the CUE (the NPP-to-GPP ratio) across multiple sites comprising forests, grassland and croplands ($n=24$) according to the management status: natural ($n=83$), elevated CO_2 ($n=7$) and fertilized ($n=25$). Inset, graph showing a higher CUE of managed sites than natural sites. Differences between the managed and natural sites were significant using a t -test. * $P < 0.05$; *** $P < 0.001$. Bars and error bars show means \pm s.d. of the CUE.

peak growth of global vegetation could be improved when independent estimations for global GPP using SIF⁵³ and/or carbonyl sulfide⁵⁴ become available as global GPP tracers in the future. The Lindeman–Merenda–Gold (LMG) method of relative importance calculation allows us to differentiate between the contributions of correlated regressors without considering regressors' order effects in a multiple linear regression⁵⁵, and has been widely used to the attributions of observation-based datasets to global environmental change factors^{12,56}, but caution should be taken when evaluating the model factorial experimental results. To address the possible saturation issue of NDVI in the tropics, we found that the $NDVI_{max}$ values might reach saturation when the maximum leaf area index (LAI_{max}) approached a range from 4 to 5 (Supplementary Fig. 14a), and most saturated $NDVI_{max}$ regions were located in tropical forest (Supplementary Fig. 14b). Although the NDVI data might be saturated and influenced by cloud cover in the tropics, our analyses of EVI_{max} data that were less influenced by clouds than NDVI showed consistently increasing trends with $NDVI_{max}$ in many regions (Supplementary Fig. 3).

Overall, this study used multiple data sources and approaches to show an increasing peak growth of global vegetation. The findings of this study have several important implications. First, our results suggest that the recent increase of global peak vegetation growth is not only driven by rising CO_2 and nitrogen deposition, but also by agricultural intensification. Second, soil carbon losses⁵⁷ caused by croplands expansion need to be considered in the prediction of future terrestrial carbon sink under the increasing peak plant growth. Lastly, the projections of future atmospheric $[CO_2]$ seasonality would benefit from a better understanding of the processes regulating peak vegetation growth, such as the seasonal dynamics of leaf photosynthetic capacity (V_{cmax})^{58–60}, deforestation²⁴, natural disturbances such as fires⁴³ and nutrient limitations⁶¹.

Methods

Flux-tower-based GPP data. We included 30-year eddy-covariance-flux-based data as large observation-based vegetation productivity datasets. The flux-tower-based GPP products (1982–2011) were provided by the Max Planck Institute for Biogeochemistry (MPI-BGC), with a spatial resolution of $0.5^\circ \times 0.5^\circ$, using the machine-learning technique MTE. FLUXNET observations of carbon dioxide, water and energy fluxes were upscaled with the trained MTE to generate global flux fields at a $0.5^\circ \times 0.5^\circ$ spatial resolution and monthly temporal resolution (<https://www.bgc-jena.mpg.de/geodb/projects/Home.php>).

Satellite-derived data. We used the biweekly GIMMS third-generation NDVI (NDVI3g; 1982–2011) dataset (available at <https://ecocast.arc.nasa.gov/data/pub/gimms/3g.v0>), with a spatial resolution of $1/12^\circ$ (~ 8 km). The GIMMS-NDVI3g data generated from the calibrated Advanced Very High Resolution Radiometer were carefully corrected for sensor degradation, intersensor differences, cloud cover, solar zenith angle, viewing angle effects due to satellite drift, and volcanic aerosols^{62,63}. Here, we investigated the long-term NDVI data, as a proxy of plant photosynthesis, to monitor the vegetation growth. First, we composited the biweekly GIMMS-NDVI3g data to monthly temporal resolution by selecting the higher of the two composites in the same month. These were then aggregated to $0.5^\circ \times 0.5^\circ$ to match the resolution of GPP data and meteorological data.

Given that NDVI data might suffer from saturation in high-biomass regions, we examined the relationship between NDVI and LAI. The GIMMS-LAI3g was derived from the GIMMS-NDVI3g dataset and Moderate Resolution Imaging Spectroradiometer (MODIS) LAI using the artificial neural network models⁶⁴. The GIMMS-LAI3g dataset provided LAI observations at 15-d temporal resolution and $1/12^\circ$ spatial resolution. First, we composited the 15-d GIMMS-LAI3g data to monthly LAI. These were then aggregated to the $0.5^\circ \times 0.5^\circ$ spatial resolution. We also used monthly MODIS EVI data (MOD13C2; collection 6), optimizing the vegetation signal with reductions in atmospheric cloud and aerosol contamination effects⁶⁵, as a complementary proxy to provide more confidence in interpreting peak vegetation growth. The monthly MODIS EVI data at 0.05° spatial resolution (2000–2011) were obtained from the online Data Pool at the National Aeronautics and Space Administration (NASA) Land Processes Distributed Active Archive Centre located at the US Geological Survey Earth Resources Observation and Science Centre (<https://lpdaac.usgs.gov>). The gridded EVI datasets include pixel-level quality assurance flags, as well as statistics of EVI quality and input data. To obtain high-quality EVI composites, we filtered the original data using the following criteria⁶⁶ based on the quality assurance layers: (1) corrected product produced at ideal quality for all bands; (2) highest quality for bands 1–7; (3) atmospheric correction; (4) adjacency correction; (5) MOD35 cloud flag indicated 'clear'; (6) no detections of cloud-shadow; and (7) low or average aerosol quantities. Gaps remaining after quality assurance filtering were filled by interpolation in the temporal dimension, computing the values of gaps by fitting linearly between the two adjacent points. The time series with more than two consecutive gaps were excluded from further analyses. The data were then mosaicked and re-projected using the MODIS Reprojection Tool, and mosaicked images were resampled into $0.5^\circ \times 0.5^\circ$ (latitude \times longitude) resolution using the nearest-neighbour algorithm.

We analysed the SIF data to investigate vegetation photosynthetic capacity at the biome level. The SIF data were produced using spectra from the GOME-2 instrument onboard the MetOp-A platform¹⁹. SIF retrievals were performed in the 715–758 nm spectral window with ~ 0.5 nm spectral resolution⁶⁷. The SIF products (https://avdc.gsfc.nasa.gov/pub/data/satellite/MetOp/GOME_F) used in this study were GOME2_F level 3 monthly retrievals (2007–2015) with a spatial resolution of $0.5^\circ \times 0.5^\circ$. The GOME-2 level 3 SIF retrievals were quality filtered, aggregated as monthly averages and gridded globally. Previous studies have reported that SIF could be a robust indicator of GPP, although the uncertainties existed in the GPP-SIF relationship^{19,68}.

Gridded GPP_{max}, NDVI_{max} and SIF_{max} datasets were compiled annually by picking out the maximum from the monthly composites of the same year in each grid cell. In particular, the long-term MTE GPP_{max} and NDVI_{max} products were identified to monitor the linear trends of global peak vegetation growth in the past three decades. The spatial patterns of temporal trends in each dataset were calculated using a least squares linear regression for each grid. All the data calculations were accomplished in R (<http://www.r-project.org/>).

Forcing datasets. Forcing datasets were involved to investigate the contribution of multiple factors to annual changes in NDVI_{max} over 1982–2010, including radiation, air temperature, precipitation, the fraction of cropland, nitrogen deposition and rising [CO₂]. Annual climatology (including air temperature and precipitation) data with a spatial resolution of $0.5^\circ \times 0.5^\circ$ were obtained from meteorological data stored at the Climate Research Unit (CRU) at the University of East Anglia (CRU TS 3.23)⁶⁹. We obtained $0.5^\circ \times 0.5^\circ$ gridded data of annual downward shortwave radiation at the surface ($W m^{-2}$) from the Terrestrial Hydrology Research Group at Princeton University⁷⁰ (<http://hydrology.princeton.edu/data/pgf/v2/0.5deg/monthly/>). The annual global gridded ($0.5^\circ \times 0.5^\circ$) cropland fraction change dataset (1982–2010) was obtained from Hurtt et al.⁷¹ (http://daac.ornl.gov/cgi-bin/dsviewer.pl?ds_id=1248) and used as the agriculture driving factor in analysing the dominators of observed peak plant growth (NDVI_{max}). Here, the global gridded ($0.5^\circ \times 0.5^\circ$) atmospheric components were change data for atmospheric nitrogen deposition and atmospheric [CO₂]. Both of the datasets were obtained from the MsTMIP environmental driver datasets for the historical period^{36,72}. The atmospheric [CO₂] data prepared for the MsTMIP were downloaded from the Oak Ridge National Laboratory Distributed Active Archive Center at a monthly time scale, then averaged to the annual mean to match the NDVI_{max} data. Based on Dentener's maps and introduced spatiotemporal variation from nitrogen emissions⁷³, time-varying annual nitrogen deposition rate (NH_x-N and NO_y-N) data were used in this study.

Relative importance calculation. We used a relative importance analysis approach to quantify the relative contributions of each factor (for example, radiation, air temperature, precipitation, the fraction of cropland, nitrogen deposition and rising CO₂) to the annual changes of NDVI_{max} in each grid cell, expressed as the Pearson correlation in a multiple linear regression ($NDVI_{max} = b_0 + b_1 \times radiation + b_2 \times temperature + b_3 \times precipitation + b_4 \times cropland\ fraction + b_5 \times nitrogen\ deposition + b_6 \times CO_2 + \epsilon$). ϵ represented other drivers that were not considered but might contribute to NDVI_{max} variation. The algorithm was performed with the 'relaimpo' package in R, which was based on variance decomposition for multiple linear regression models⁷⁴. The 'relaimpo' package provides six different methods for analysing the relative importance of each regressor in linear regression. We chose one of the most computer-intensive and commonly used methods named 'LMG', which allows differentiation of the contribution of different correlated regressors in a multiple linear regression. In multiple regression models, the relative importance assessment strongly depended on the order of the regressors. The LMG method estimated the relative importance (RI) of each variable by decomposing the sum of squares into non-negative contributions shared by each variable, and the LMG values were obtained by averaging the sequential sum of squares (r^2) for all possible orders. Finally, all RI values were normalized (divided by r^2) to sum to 1.

In each grid cell, we calculated the contributions of each factor to interannual NDVI_{max} (Supplementary Fig. 4). Then, the global attributions to NDVI_{max} were calculated by averaging the values of contributors at the pixel level (statistically significant pixels; $P < 0.05$).

In situ observation dataset. To test whether crops have higher photosynthetic capacity than natural plant species, we investigated the measured leaf-level maximum carboxylation rate (V_{cmax}) and flux-tower-observed GPP_{max} at the ecosystem level, which were analysed using the probability density function. The leaf-level maximum carboxylation rate (V_{cmax} , $\mu mol m^{-2} s^{-1}$) data of 612 observations across 81 plant species were compiled from the TRY database¹⁵ (<http://www.try-db.org>)—a coverage of plant trait data representing plant functional diversity at the global scale. Leaf V_{cmax} data were then divided into crops, trees and grasses to explore the differences in probability density among species^{21–23}. Photosynthetic capacity simulations within earth system models were closely associated with V_{cmax} ⁴⁵. The measured multi-species leaf V_{cmax} in Fig. 3a indicates the overall difference in leaf-level plant photosynthetic capacity differences across crops, trees and grasses.

We also used eddy-covariance-flux-tower data from 125 flux sites (including forest, grassland and cropland) across the globe (see Supplementary Data 1 for a full list). These GPP flux data were obtained from the FLUXNET2015 Tier 1 dataset (November 2016 release; <http://fluxnet.fluxdata.org/data/fluxnet2015-dataset/>). Flux-tower GPP values were calculated as the mean of both daytime and night-time partition methods after a data quality check. According to the methods and criteria in Reichstein et al.⁷⁵ and Papale et al.⁷⁶, data for each site year in the database were filtered. Due to the inevitable data uncertainties arising from indirect measurement and some negative values in some site years, only site years with more than 300 daily estimates were chosen from the database. There were 960 site years of GPP data in total. Comprehensive fit functions and algorithms were developed to derive the flux-tower GPP_{max} of each site in different biomes. Details on the flux GPP_{max} calculation methods are described in Xia et al.¹⁰.

Meta-analysis of leaf biomass data. We conducted a systematic meta-analysis to further explain the higher contributions of atmospheric [CO₂] and nitrogen deposition relative to climate change on NDVI_{max}, according to the guidelines listed in the PRISMA (preferred reporting items for systematic reviews and meta-analyses) statement (<http://www.prisma-statement.org/>). We searched peer-reviewed and primary research papers before December 2016 from the Web of Science. Candidate papers were individually examined for data meeting the following criteria: (1) both control and treatment existed; (2) the responses of terrestrial plant growth to changes in environmental factors (CO₂, nitrogen and temperature) were provided at the species level, and the means (X), sample sizes (n), and s.d. or s.e.m. values under the control and treatment were also provided; and (3) the examined responsive variables encompassed plant parts; for example, whole, aboveground, belowground, leaf, root, stem, and so on. Since sample sizes and variance of the original studies were included in our data collections, our meta-analysis followed the guidelines set by Vetter et al.⁷⁷. Based on these guidelines, a database of 466 studies (see Supplementary Data 2 for a full list) investigating the response of plant growth under treatment (warming, nitrogen addition and elevated CO₂) was established for further analysis (Supplementary Fig. 6). Here, we further examined the responses of leaf biomass to warming, nitrogen addition and elevated CO₂ using this database. Moreover, we separated the experimental data into different plant functional types (woody, herb, tree, shrub, grass or forb) and climatic zones (tropical, temperate or boreal). Overall, our meta-analysis considered leaf-growth data from 92 observations for warming, 234 observations for nitrogen addition and 113 observations for elevated CO₂.

For the studies that provided s.e.m., s.d. was calculated by:

$$s.d. = s.e.m. \cdot \sqrt{n} \quad (1)$$

The meta-analysis followed the techniques described in Hedges et al.⁷⁸. The response of leaf growth to treatments was estimated using the natural log-transformed response ratio (RR):

$$\ln[\text{RR}] = \ln[X_T / X_C] \quad (2)$$

where X_C is the mean value of leaf biomass under the control treatment and X_T denotes the mean value of the corresponding treatment (warming, nitrogen addition or elevated CO_2). The variance of the natural log-transformed response ratio was:

$$v = \left(\frac{\text{s.d.}_C^2}{n_C X_C^2} + \frac{\text{s.d.}_T^2}{n_T X_T^2} \right) \quad (3)$$

where s.d._C and s.d._T are the s.d. values of X_C and X_T , and n_C and n_T are the sample sizes of X_C and X_T , respectively.

Then, a mixed-effects model was used to obtain the weighted response ratio of leaf growth to warming, nitrogen addition and elevated CO_2 , respectively. The weighted response ratio (RR_{++}) was calculated as below (m and k are the number of groups and comparison, respectively):

$$\text{RR}_{++} = \frac{\sum_{i=1}^m \sum_{j=1}^k W_{ij} \text{RR}_{ij}}{\sum_{i=1}^m \sum_{j=1}^k W_{ij}} \quad (4)$$

where W is the weight ($1/v$) of each RR, and its s.e.m. was calculated as below:

$$S(\text{RR}_{++}) = \sqrt{\frac{1}{\sum_{i=1}^m \sum_{j=1}^k W_{ij}}} \quad (5)$$

The 95% CI was $\text{RR}_{++} \pm 1.96 \times S(\text{RR}_{++})$, and was generated by bootstrapping the data using MetaWin 2.1 (Sinauer Associates). The results were back-transformed and are represented as percentage change by $(\exp(\text{RR}_{++}) - 1) \times 100\%$. The response was considered significant if the 95% CI did not overlap with zero.

Processing model outputs from MsTMIP. To further evaluate the simulated global peak vegetation growth trends and their driving factors, GPP_{max} of 15 MsTMIP models were used during 1982–2010. The models were forced with consistent driver datasets. The simulation protocol and details of the forcing data were described by Huntzinger et al.²⁰ and Wei et al.³⁶. We performed a series of experimental simulations to analyse the four main drivers (climate change, LCC, CO_2 fertilization and nitrogen deposition) of simulated global peak vegetation growth: initial conditions, with all environmental drivers constant (RG1); varying climate (temperature, precipitation and radiation) only (SG1); varying climate and land cover (SG2); varying climate, land cover and CO_2 (SG3); and varying climate, land cover, CO_2 and nitrogen deposition (BG1). Simulations SG1-RG1, SG2-SG1, SG3-SG2 and BG1-SG3 were used to evaluate the effects of climate change, LCC, CO_2 fertilization and nitrogen deposition on peak vegetation growth, respectively. It should be noted that not all 15 models submitted all 4 sensitivity simulations, especially for nitrogen deposition (Supplementary Table 1). Thus, we conducted the factorial experiments in two sub-ensembles: eight models with nitrogen limitation (+nitrogen) and seven models without nitrogen limitation (–nitrogen). An attribution analysis for each individual model in the sub-ensembles was completed, then values were averaged across the models. Additionally, current model intercomparison projects consider the climate change scenario (SG1) as a combination of temperature, precipitation and radiation, making direct comparison with the relative importance calculations less comprehensive. We recommend that future model intercomparison projects request outputs from model simulations under a separated climate factor scenario to allow for more direct comparisons with observation-based attributions. We also request a possible scenario incorporating a combination of varying climate and varying CO_2 to attribute the LCC effect in future model intercomparison experiments.

Carbon use efficiency (CUE) dataset. The CUE was calculated as the ratio of NPP to GPP. Both in situ GPP and NPP data were obtained from the database in DeLucia et al.⁷⁹, Campioli et al.⁸⁰ and Chen et al.⁸¹. Here, we present a CUE dataset of 139 site years (Supplementary Fig. 15) comprising forests, grasslands and croplands. According to the management status and treatments, sites were divided into natural, elevated CO_2 and fertilized.

Reporting Summary. Further information on research design is available in the Nature Research Reporting Summary linked to this article.

Code availability. The code used to generate the results of this study are available from the corresponding author upon request.

Data availability

The MTE GPP datasets are available at <https://www.bgc-jena.mpg.de/geodb/projects/Home.php>. The Advanced Very High Resolution Radiometer GIMMS-

NDVI3g datasets are available at <https://ecocast.arc.nasa.gov/data/pub/gimms/3g.v0>. The GOME-2 SIF datasets are available at https://avdc.gsfc.nasa.gov/pub/data/satellite/MetOp/GOME_F. The MODIS EVI data are available from the NASA Land Processes Distributed Active Archive Center at <https://lpdaac.usgs.gov>. The in situ GPP observations are available from FLUXNET2015 at <http://fluxnet.fluxdata.org/data/fluxnet2015-dataset/>. The V_{cmax} data are available from the TRY database¹⁵ at <http://www.try-db.org>. The CRU TS 3.23 climate datasets are available from the CRU (<https://crudata.uea.ac.uk/cru/data/hrg/>). The shortwave radiation datasets are available from the Terrestrial Hydrology Research Group at <http://hydrology.princeton.edu/data/pgf/v2/0.5deg/monthly/>. The MsTMIP modelling results are available at <https://nacp.ornl.gov/mstmpdata/>.

Received: 31 July 2017; Accepted: 5 October 2018;

Published online: 12 November 2018

References

- Ahlström, A. et al. The dominant role of semi-arid ecosystems in the trend and variability of the land CO_2 sink. *Science* **348**, 895–899 (2015).
- Randerson, J. T., Thompson, M. V., Conway, T. J., Fung, I. Y. & Field, C. B. The contribution of terrestrial sources and sinks to trends in the seasonal cycle of atmospheric carbon dioxide. *Glob. Biogeochem. Cycles* **11**, 535–560 (1997).
- Keeling, C. D., Chin, J. F. S. & Whorf, T. P. Increased activity of northern vegetation inferred from atmospheric CO_2 measurements. *Nature* **382**, 146–149 (1996).
- Myneni, R. B., Keeling, C. D., Tucker, C. J., Asrar, G. & Nemani, R. R. Increased plant growth in the northern high latitudes from 1981 to 1991. *Nature* **386**, 698–702 (1997).
- Lucht, W. et al. Climatic control of the high-latitude vegetation greening trend and Pinatubo effect. *Science* **296**, 698–702 (1997).
- Nemani, R. R. et al. Climate-driven increases in global terrestrial net primary production from 1982 to 1999. *Science* **300**, 1560–1563 (2003).
- Xu, L. et al. Temperature and vegetation seasonality diminishment over northern lands. *Nat. Clim. Change* **3**, 581–586 (2013).
- Forkel, M. et al. Enhanced seasonal CO_2 exchange caused by amplified plant productivity in northern ecosystems. *Science* **351**, 696–699 (2016).
- Graven, H. D. et al. Enhanced seasonal exchange of CO_2 by northern ecosystems since 1960. *Science* **341**, 1085–1089 (2013).
- Xia, J. et al. Joint control of terrestrial gross primary productivity by plant phenology and physiology. *Proc. Natl Acad. Sci. USA* **112**, 2788–2793 (2015).
- Zhou, S. et al. Explaining inter-annual variability of gross primary productivity from plant phenology and physiology. *Agric. For. Meteorol.* **226**, 246–256 (2016).
- Musavi, T. et al. Stand age and species richness dampen interannual variation of ecosystem-level photosynthetic capacity. *Nat. Ecol. Evol.* **1**, 0048 (2017).
- Zhu, Z. et al. Greening of the Earth and its drivers. *Nat. Clim. Change* **6**, 791–795 (2016).
- Anav, A. et al. Spatiotemporal patterns of terrestrial gross primary production: a review. *Rev. Geophys.* **53**, 2015RG000483 (2015).
- Kattge, J. et al. TRY—a global database of plant traits. *Glob. Change Biol.* **17**, 2905–2935 (2011).
- Stein, W. E., Mannolini, F., Hernick, L. V., Landing, E. & Berry, C. M. Giant cladoxylopsid trees resolve the enigma of the Earth's earliest forest stumps at Gilboa. *Nature* **446**, 904–907 (2007).
- Jung, M. et al. Global patterns of land-atmosphere fluxes of carbon dioxide, latent heat, and sensible heat derived from eddy covariance, satellite, and meteorological observations. *J. Geophys. Res. Biogeosci.* **116**, G00J07 (2011).
- Hickler, T. et al. Precipitation controls Sahel greening trend. *Geophys. Res. Lett.* **32**, L21415 (2005).
- Guanter, L. et al. Global and time-resolved monitoring of crop photosynthesis with chlorophyll fluorescence. *Proc. Natl Acad. Sci. USA* **111**, 1327–1333 (2014).
- Huntzinger, D. N. et al. The North American Carbon Program Multi-Scale Synthesis and Terrestrial Model Intercomparison Project—Part 1: overview and experimental design. *Geosci. Model Dev.* **6**, 2121–2133 (2013).
- Medlyn, B. E. et al. Effects of elevated $[\text{CO}_2]$ on photosynthesis in European forest species: a meta-analysis of model parameters. *Plant Cell Environ.* **22**, 1475–1495 (1999).
- Montgomery, R. A. & Givnish, T. J. Adaptive radiation of photosynthetic physiology in the Hawaiian lobeliads: dynamic photosynthetic responses. *Oecologia* **155**, 455–467 (2008).
- Wilson, K. B., Baldocchi, D. D. & Hanson, P. J. Spatial and seasonal variability of photosynthetic parameters and their relationship to leaf nitrogen in a deciduous forest. *Tree Physiol.* **20**, 565–578 (2000).
- Zeng, N. et al. Agricultural Green Revolution as a driver of increasing atmospheric CO_2 seasonal amplitude. *Nature* **515**, 394–397 (2014).
- Schimel, D., Stephens, B. B. & Fisher, J. B. Effect of increasing CO_2 on the terrestrial carbon cycle. *Proc. Natl Acad. Sci. USA* **112**, 436–441 (2015).

26. Ainsworth, E. A. & Long, S. P. What have we learned from 15 years of free-air CO₂ enrichment (FACE)? A meta-analytic review of the responses of photosynthesis, canopy properties and plant production to rising CO₂. *New Phytol.* **165**, 351–371 (2005).
27. Luo, Y. Q., Hui, D. F. & Zhang, D. Q. Elevated CO₂ stimulates net accumulations of carbon and nitrogen in land ecosystems: a meta-analysis. *Ecology* **87**, 53–63 (2006).
28. LeBauer, D. S. & Treseder, K. K. Nitrogen limitation of net primary productivity in terrestrial ecosystems is globally distributed. *Ecology* **89**, 371–379 (2008).
29. Xia, J. Y. & Wan, S. Q. Global response patterns of terrestrial plant species to nitrogen addition. *New Phytol.* **179**, 428–439 (2008).
30. Piao, S. et al. Leaf onset in the Northern Hemisphere triggered by daytime temperature. *Nat. Commun.* **6**, 6911 (2015).
31. Niu, S. L. et al. Water-mediated responses of ecosystem carbon fluxes to climatic change in a temperate steppe. *New Phytol.* **177**, 209–219 (2008).
32. Xia, J. Y., Niu, S. L. & Wan, S. Q. Response of ecosystem carbon exchange to warming and nitrogen addition during two hydrologically contrasting growing seasons in a temperate steppe. *Glob. Change Biol.* **15**, 1544–1556 (2009).
33. Rustad, L. et al. A meta-analysis of the response of soil respiration, net nitrogen mineralization and aboveground plant growth to experimental ecosystem warming. *Oecologia* **126**, 543–562 (2001).
34. Huntzinger, D. N. et al. *NACP MsTMIP: Global 0.5-degree Model Outputs in Standard Format, Version 1.0* (ORNL DAAC, 2016); <https://doi.org/10.3334/ORNLDAAC/1225>
35. Thomas, R. T. et al. Increased light-use efficiency in northern terrestrial ecosystems indicated by CO₂ and greening observations. *Geophys. Res. Lett.* **43**, 11339–11349 (2016).
36. Wei, Y. et al. The North American Carbon Program Multi-scale Synthesis and Terrestrial Model Intercomparison Project—Part 2: environmental driver data. *Geosci. Model Dev.* **7**, 2875–2893 (2014).
37. Gray, J. M. et al. Direct human influence on atmospheric CO₂ seasonality from increased cropland productivity. *Nature* **515**, 398–401 (2014).
38. Wenzel, S., Cox, P. M., Eyring, V. & Friedlingstein, P. Projected land photosynthesis constrained by changes in the seasonal cycle of atmospheric CO₂. *Nature* **538**, 499–501 (2016).
39. Magnani, F. et al. The human footprint in the carbon cycle of temperate and boreal forests. *Nature* **447**, 849–851 (2007).
40. Guan, K. et al. Photosynthetic seasonality of global tropical forests constrained by hydroclimate. *Nat. Geosci.* **8**, 284–289 (2015).
41. Sacks, W. J., Cook, B. I., Buening, N., Levis, S. & Helkowski, J. H. Effects of global irrigation on the near-surface climate. *Clim. Dynam.* **33**, 159–175 (2009).
42. Zhang, X. et al. Managing nitrogen for sustainable development. *Nature* **528**, 51–59 (2015).
43. Zhao, F. et al. Role of CO₂, climate and land use in regulating the seasonal amplitude increase of carbon fluxes in terrestrial ecosystems: a multimodel analysis. *Biogeosciences* **13**, 5121–5137 (2016).
44. Fernández-Martínez, M. et al. Atmospheric deposition, CO₂, and change in the land carbon sink. *Sci. Rep.* **7**, 9632 (2017).
45. Ali, A. A. et al. Global-scale environmental control of plant photosynthetic capacity. *Ecol. Appl.* **25**, 2349–2365 (2015).
46. Stith, S. et al. Evaluation of the terrestrial carbon cycle, future plant geography and climate-carbon cycle feedbacks using five dynamic global vegetation models (DGVMs). *Glob. Change Biol.* **14**, 2015–2039 (2008).
47. Bondeau, A. et al. Modelling the role of agriculture for the 20th century global terrestrial carbon balance. *Glob. Change Biol.* **13**, 679–706 (2007).
48. Gervois, S. et al. Including croplands in a global biosphere model: methodology and evaluation at specific sites. *Earth Interact.* **8**, 1–25 (2004).
49. Han, J., Chen, J., Miao, Y. & Wan, S. Multiple resource use efficiency (mRUE): a new concept for ecosystem production. *Sci. Rep.* **6**, 37453 (2016).
50. Lawrence, D. M. et al. The Land Use Model Intercomparison Project (LUMIP) contribution to CMIP6: rationale and experimental design. *Geosci. Model Dev.* **9**, 2973–2998 (2016).
51. Chen, M. et al. Regional contribution to variability and trends of global gross primary productivity. *Environ. Res. Lett.* **12**, 105005 (2016).
52. Running, S. W. A measurable planetary boundary for the biosphere. *Science* **337**, 1458–1459 (2012).
53. Sun, Y. et al. OCO-2 advances photosynthesis observation from space via solar induced chlorophyll fluorescence. *Science* **358**, eaam5747 (2017).
54. Hilton, T. W. et al. Peak growing season gross uptake of carbon in North America is largest in the Midwest USA. *Nat. Clim. Change* **7**, 450–454 (2017).
55. Yao, Y. et al. Spatiotemporal pattern of gross primary productivity and its covariation with climate in China over the last thirty years. *Glob. Change Biol.* **24**, 184–196 (2018).
56. Carvahalais, N. et al. Global covariation of carbon turnover times with climate in terrestrial ecosystems. *Nature* **514**, 213–217 (2014).
57. Sanderman, J., Hengl, T. & Fiske, G. J. Soil carbon debt of 12,000 years of human land use. *Proc. Natl Acad. Sci. USA* **114**, 9575–9580 (2017).
58. Croft, H. et al. Leaf chlorophyll content as a proxy for leaf photosynthetic capacity. *Glob. Change Biol.* **23**, 3513–3524 (2017).
59. Luo, X. et al. Incorporating leaf chlorophyll content into a two-leaf terrestrial biosphere model for estimating carbon and water fluxes at a forest site. *Agric. For. Meteorol.* **248**, 156–168 (2018).
60. Alton, P. B. Retrieval of seasonal RuBisCO-limited photosynthetic capacity at global FLUXNET sites from hyperspectral satellite remote sensing: impact on carbon modelling. *Agric. For. Meteorol.* **232**, 74–88 (2017).
61. Wieder, W. R., Cleveland, C. C., Smith, W. K. & Todd-Brown, K. Future productivity and carbon storage limited by terrestrial nutrient availability. *Nat. Geosci.* **8**, 441–444 (2015).
62. Piao, S. et al. Evidence for a weakening relationship between interannual temperature variability and northern vegetation activity. *Nat. Commun.* **5**, 5018 (2014).
63. Tucker, C. J. et al. An extended AVHRR 8-km NDVI dataset compatible with MODIS and SPOT vegetation NDVI data. *Int. J. Remote Sens.* **26**, 4485–4498 (2005).
64. Zhu, Z. C. et al. Global data sets of vegetation leaf area index (LAI)3g and fraction of photosynthetically active radiation (FPAR)3g derived from Global Inventory Modeling and Mapping Studies (GIMMS) Normalized Difference Vegetation Index (NDVI3g) for the period 1982 to 2011. *Remote Sens.* **5**, 927–948 (2013).
65. Huete, A. et al. Overview of the radiometric and biophysical performance of the MODIS vegetation indices. *Remote Sens. Environ.* **83**, 195–213 (2002).
66. Ma, X., Huete, A., Moran, S., Ponce-Campos, G. & Eamus, D. Abrupt shifts in phenology and vegetation productivity under climate extremes. *J. Geophys. Res. Biogeosci.* **120**, 2036–2052 (2015).
67. Joiner, J. et al. Global monitoring of terrestrial chlorophyll fluorescence from moderate-spectral-resolution near-infrared satellite measurements: methodology, simulations, and application to GOME-2. *Atmos. Meas. Tech.* **6**, 2803–2823 (2013).
68. Parazoo, N. C. et al. Interpreting seasonal changes in the carbon balance of southern Amazonia using measurements of XCO₂ and chlorophyll fluorescence from GOSAT. *Geophys. Res. Lett.* **40**, 2829–2833 (2013).
69. Harris, I., Jones, P. D., Osborn, T. J. & Lister, D. H. Updated high-resolution grids of monthly climatic observations—the CRU TS 3.10 dataset. *Int. J. Climatol.* **34**, 623–642 (2014).
70. Sheffield, J., Goteti, G. & Wood, E. F. Development of a 50-year high-resolution global dataset of meteorological forcings for land surface modeling. *J. Clim.* **19**, 3088–3111 (2006).
71. Hurtt, G. C. et al. Harmonization of land-use scenarios for the period 1500–2100: 600 years of global gridded annual land-use transitions, wood harvest, and resulting secondary lands. *Clim. Change* **109**, 117–161 (2011).
72. Wei, Y. et al. *NACP MsTMIP: Global and North American Driver Data for Multi-Model Intercomparison* (ORNL DAAC, 2014); <https://doi.org/10.3334/ORNLDAAC/1220>
73. Dentener, F. J. *Global Maps of Atmospheric Nitrogen Deposition, 1860, 1993, and 2050* (ORNL DAAC, 2006); <https://doi.org/10.3334/ORNLDAAC/830>
74. Grömping, U. Relative importance for linear regression in R: the package relaimpo. *J. Stat. Softw.* **17**, 1–27 (2006).
75. Reichstein, M. et al. On the separation of net ecosystem exchange into assimilation and ecosystem respiration: review and improved algorithm. *Glob. Change Biol.* **11**, 1424–1439 (2005).
76. Papale, D. et al. Towards a standardized processing of net ecosystem exchange measured with eddy covariance technique: algorithms and uncertainty estimation. *Biogeosciences* **3**, 571–583 (2006).
77. Vetter, D., Rücker, G. & Storch, I. Meta-analysis: a need for well-defined usage in ecology and conservation biology. *Ecosphere* **4**, 1–24 (2013).
78. Hedges, L. V., Gurevitch, J. & Curtis, P. S. The meta-analysis of response ratios in experimental ecology. *Ecology* **80**, 1150–1156 (1999).
79. DeLucia, E. H., Drake, J. E., Thomas, R. B. & Gonzalez-Meler, M. Forest carbon use efficiency: is respiration a constant fraction of gross primary production? *Glob. Change Biol.* **13**, 1157–1167 (2007).
80. Campioli, M. et al. Biomass production efficiency controlled by management in temperate and boreal ecosystems. *Nat. Geosci.* **8**, 843–846 (2015).
81. Chen, Z., Yu, G. & Wang, Q. Ecosystem carbon use efficiency in China: variation and influence factors. *Ecol. Indic.* **90**, 316–323 (2018).

Acknowledgements

This work was financially supported by the National Key R&D Program of China (2017YFA0604603), National Natural Science Foundation (31430015, 41601099 and 41630528) and National 1000 Young Talents Program of China. We thank all the people who worked to provide data for this study, particularly the MsTMIP modelling group. We are grateful for receiving MTE GPP products from MPI-BGC, biweekly NDVI data from the GIMMS team, MODIS EVI products from USGS, climate-forcing data from CRU and Princeton University, CO₂ site data from NOAA, and GOME-2 SIF retrievals from Eumetsat. We further thank the TRY initiative for plant traits (<http://www.try-db.org>). The TRY initiative and database are hosted, developed and maintained by J. Kattge and G. Bönisch (MPI-BGC). The eddy-covariance data of FLUXNET used in this study

were mainly acquired by the following networks: AmeriFlux, GHG-Europe, SOERE, FORE-T, the Fluxnet-Canada Research Network (supported by CFCAS, NSERC, BIOCAP, Environment Canada and NRCan), GreenGrass, KoFlux, LBA, NECC, OzFlux, TCOS-Siberia and USCCC. The vector map data were made using Natural Earth. J.B.F. contributed to this paper from the Jet Propulsion Laboratory, California Institute of Technology, under a contract with NASA, and support was provided by the IDS programme.

Author contributions

J.X. designed the study. K.H. performed the analysis. J.X. and K.H. wrote the first draft. Y.L., Y.Wang, A.A., J.C., E.C., Z.L., J.W., Y.Q., X.X., L.Y. and C.B. contributed to the idea development. C.S., D.N.H., R.B.C., Y.F., J.B.F., A.M.M., K.S. and Y.Wei provided the modelling results. All authors interpreted the results and revised the manuscript.

Competing interests

The authors declare no competing interests.

Additional information

Supplementary information is available for this paper at <https://doi.org/10.1038/s41559-018-0714-0>.

Reprints and permissions information is available at www.nature.com/reprints.

Correspondence and requests for materials should be addressed to J.X.

Publisher's note: Springer Nature remains neutral with regard to jurisdictional claims in published maps and institutional affiliations.

© The Author(s), under exclusive licence to Springer Nature Limited 2018

Reporting Summary

Nature Research wishes to improve the reproducibility of the work that we publish. This form provides structure for consistency and transparency in reporting. For further information on Nature Research policies, see [Authors & Referees](#) and the [Editorial Policy Checklist](#).

Statistical parameters

When statistical analyses are reported, confirm that the following items are present in the relevant location (e.g. figure legend, table legend, main text, or Methods section).

n/a Confirmed

- The exact sample size (n) for each experimental group/condition, given as a discrete number and unit of measurement
- An indication of whether measurements were taken from distinct samples or whether the same sample was measured repeatedly
- The statistical test(s) used AND whether they are one- or two-sided
Only common tests should be described solely by name; describe more complex techniques in the Methods section.
- A description of all covariates tested
- A description of any assumptions or corrections, such as tests of normality and adjustment for multiple comparisons
- A full description of the statistics including central tendency (e.g. means) or other basic estimates (e.g. regression coefficient) AND variation (e.g. standard deviation) or associated estimates of uncertainty (e.g. confidence intervals)
- For null hypothesis testing, the test statistic (e.g. F , t , r) with confidence intervals, effect sizes, degrees of freedom and P value noted
Give P values as exact values whenever suitable.
- For Bayesian analysis, information on the choice of priors and Markov chain Monte Carlo settings
- For hierarchical and complex designs, identification of the appropriate level for tests and full reporting of outcomes
- Estimates of effect sizes (e.g. Cohen's d , Pearson's r), indicating how they were calculated
- Clearly defined error bars
State explicitly what error bars represent (e.g. SD, SE, CI)

Our web collection on [statistics for biologists](#) may be useful.

Software and code

Policy information about [availability of computer code](#)

Data collection No software was used for data collection.

Data analysis We used Metawin 2.1 and the R version 3.3.1.

For manuscripts utilizing custom algorithms or software that are central to the research but not yet described in published literature, software must be made available to editors/reviewers upon request. We strongly encourage code deposition in a community repository (e.g. GitHub). See the Nature Research [guidelines for submitting code & software](#) for further information.

Data

Policy information about [availability of data](#)

All manuscripts must include a [data availability statement](#). This statement should provide the following information, where applicable:

- Accession codes, unique identifiers, or web links for publicly available datasets
- A list of figures that have associated raw data
- A description of any restrictions on data availability

A data availability statement was presented in the manuscript. The data of all the analyzes are either publicly accessible or are available upon request.

Field-specific reporting

Please select the best fit for your research. If you are not sure, read the appropriate sections before making your selection.

Life sciences Behavioural & social sciences Ecological, evolutionary & environmental sciences

For a reference copy of the document with all sections, see [nature.com/authors/policies/ReportingSummary-flat.pdf](https://www.nature.com/authors/policies/ReportingSummary-flat.pdf)

Ecological, evolutionary & environmental sciences study design

All studies must disclose on these points even when the disclosure is negative.

Study description	This study presents an observational evidence that the peak vegetation growth has been increasing in the past three decades, based on the global satellite data and observation-based flux data sets.
Research sample	We used the satellite-derived NDVI data, GPP flux data, SIF data and climate data over the global lands. The spatial resolution of each global data set determines the number of pixels used in the study.
Sampling strategy	We defined the groups based on the existing biome maps and plant species.
Data collection	Global remote sensing data, climate data and in-situ observational data were downloaded from the URLs stated in the article. 466 eligible studies for meta-analysis were found using Web of Science.
Timing and spatial scale	The global GPP, GIMMS NDVI and climate data used in our study were from 1982 to 2011 at a 0.5 degree spatial resolution and a monthly temporal resolution. The MODIS EVI data were provided at a 0.5 degree spatial resolution and a monthly temporal resolution over 2000-2011. The SIF products were GOME2_F level 3 monthly retrievals at a 0.5 degree spatial resolution during 2007-2015. Research papers published before December 2016 from Web of Science were used in the meta-analysis.
Data exclusions	No data were excluded from the data sets in all the analyses.
Reproducibility	Our analyses were mainly based on public satellite products and observational data, and the results could be reproduced.
Randomization	We performed the global trend analysis for each pixel with satellite images and GPP data set, thus randomization is not relevant to our study.
Blinding	The majority of our study were based on existing data, therefore blinding is not relevant to our study.
Did the study involve field work?	<input type="checkbox"/> Yes <input checked="" type="checkbox"/> No

Reporting for specific materials, systems and methods

Materials & experimental systems

n/a	Involvement in the study
<input checked="" type="checkbox"/>	<input type="checkbox"/> Unique biological materials
<input checked="" type="checkbox"/>	<input type="checkbox"/> Antibodies
<input checked="" type="checkbox"/>	<input type="checkbox"/> Eukaryotic cell lines
<input checked="" type="checkbox"/>	<input type="checkbox"/> Palaeontology
<input checked="" type="checkbox"/>	<input type="checkbox"/> Animals and other organisms
<input checked="" type="checkbox"/>	<input type="checkbox"/> Human research participants

Methods

n/a	Involvement in the study
<input checked="" type="checkbox"/>	<input type="checkbox"/> ChIP-seq
<input checked="" type="checkbox"/>	<input type="checkbox"/> Flow cytometry
<input checked="" type="checkbox"/>	<input type="checkbox"/> MRI-based neuroimaging